ORIGINAL RESEARCH

Size-controlled synthesis of gold nanoparticles and related molecular imaging contrast for computed tomography

Linh Thi Ngoc Nguyen · Hieu Van Vu · Tam The Le

Abstract The discovery and development of novel contrast agents for CT imaging could address the current limitations of this non-invasive testing technique, thus improving diagnostic efficiency. Although this approach is significant to clinical research, finding a highly potent and biocompatible contrast agent is challenging. In our study, the homogeneous and monodisperse Au nanospheres were successfully synthesized using chemical reduction. The influence of surfactants, oleylamine (OLA) and sodium oleate (SOA); solvent; and reaction time on the materials' formation, size, and properties was examined to find the optimal conditions. Investigation showed that using OLA and SOA as surfactants resulted in materials with similar morphology and uniformity. The solvent 1-octadecene (ODE) and reaction time in the 30–60-min range facilitated the formation of uniform and monodisperse gold nanoparticles (GNPs). Characterization indicated that the fabricated Au materials were crystalline and spherical with a face-centered cubic (fcc) structure and an average size of 8.4–20.7 nm. Their maximum surface plasmon resonance (SPR) absorbance varied in the range of 516–531 nm. After surface modification by the poly(maleic anhydride-alt-1-octadecene) (PMAO), the Au NPs were highly stable in a aqueous solution with a zeta potential ranging from −45.6 to −42 mV, dynamic light scattering (DLS) size of 17.7 and 26.8 corresponding to the sample size of 8.4 nm and 15.5 nm, respectively. In vitro CT imaging results show that the material Au@PMAO enhanced the CT image contrast signals. Particularly, the smaller GNPs exhibited higher X-ray attenuation than the large ones. At the same investigated concentration, the image contrast performance of the Au@PMAO NPs outweighed that of the commercial product Xenetix, which contained iodine. These outstanding properties prove that the Au@PMAO material is a promising alternative for CT imaging techniques.

L. T. N. Nguyen · H. Van Vu
Faculty of Chemistry, Thai Nguyen University of Sciences, Thai Nguyen University, Tan Thinh Ward, Thai Nguyen City, Vietnam

H. Van Vu
Phong Chau Hight School, 14 Hung Son, Lam Thao, Phu Tho, Vietnam

T. T. Le (✉)
School of Chemistry, Biology and Enviroment, Vinh University, 182 Le Duan, Vinh, Vietnam
e-mail: tamlt@vinhuni.edu.vn

Introduction

Computed tomography (CT) imaging is a clinical imaging technique using X-ray sources and detectors

to generate images. The CT images can be obtained quickly and have high spatial resolution [1, 2]. This technique is a non-invasive medical diagnostic tool, providing 3D anatomical information of specific tissues and organs of the body [2–5]. CT imaging approach is based on the different attenuation of X-ray photons caused by other tissues. The number of atoms and electron density of tissues determines the attenuation coefficient. The greater the number of atoms and the more intense the electron density, the higher the attenuation degree. However, compared with other diagnostic imaging methods, such as magnetic resonance imaging (MRI), the X radiation of the photon energy spectrum used in CT is attenuated strongly by bones and rarely by soft tissues [6]. Nonetheless, CT imaging plays a crucial role in clinical and research settings. Therefore, biomedical researchers have tried to develop new contrast agents for CT imaging [7–9].

The contrast agents used for CT imaging are commonly high atomic number (Z) elements because the X-ray absorption or diffraction area is directly proportional to Z^3. The CT contrast agents provide additional vascular anatomy and describe how the blood flows in vessels [10]. In CT imaging, since the X-ray absorption or scattering cross-sectional area is directly proportional to the atomic number, the contrast agents for CT imaging are usually compounds of high atomic number elements, such as gold [7, 11–14], bismuth [15] or iodine [16–18], barium sulfate suspensions [19], and gadolinium [20]. However, these existing contrast agents provide limited information; they are suboptimal for new X-ray imaging technique and they are developing safety concerns [21]. Among those, the intravenous contrast agents which are approved by the US Food and Drug Administration (FDA) for CT imaging are iodine-based compounds such as iopamidol, xenetix, or iodixanol [16–18]. Unfortunately, an increasing number of adverse reactions caused by iodine-containing contrast agents have been reported annually [22]. Moreover, the iodine complexes have a very short circulation time in the blood. They are rapidly eliminated from the circulatory system through kidneys, thus not suitable for cases requiring long imaging times [23]. Furthermore, the physiological information obtained from iodine-based contrast agents is limited to the vascular system and large organs [10]. Other disadvantages of iodine complexes are due to their high permeability at high concentrations, causing nephrotoxicity [24–26] or skin irritation [27]. As a consequence of these drawbacks, there is growing interest in developing alternative contrast agents for CT imaging. Formulations based on nanoparticles are one of the main approaches [7, 11]. The nanoparticles-based contrast agents have the upper hand compared with the contrast agents containing iodine. Specifically, nanoparticles can load more contrast materials [7], controllable shape, size, and surface chemistry for different biomedical applications [28]. The nanoparticles-based contrast agents can stay in the bloodstream for several hours, while the circulation time of small molecules such as iodine complexes is measured in minutes [29, 30]. As such, nanoparticles-based CT contrast agents with high performance, low toxicity, and minimum dosage have become urgently needed [21]. When designing CT contrast agents, it is important to take into account general requirements: (1) the novel contrast agent should be able to improve the visualisation performance by increasing the CT attenuation difference between the target tissue and its surroundings; (2) at the used concentrations for imaging, the contrast agent should be non-toxic and biocompatible; and (3) the circulation time should be long enough to ensure the imaging efficiency [31–33].

If the iodine-based contrast agents are prohibited [34], Gd compounds can be used instead. Even though the main application of Gd compounds is for magnetic resonance imaging (MRI), they may enhance the CT imaging contrast by reasons of high atomic number and electron density. However, the CT imaging contrast obtained by Gd-based agents was lower than that by the common iodine complexes [20]. Side effects commonly appear in the kidneys and pancreas of patients using Gd^{3+} complexes [35]. Therefore, Gd-based contrast agents are not considered an ideal alternative.

Numerous proposals have been made for using gold nanoparticles (GNPs) for biomedical purposes, including CT contrast agents [9, 21, 36]. Because of the high atomic number ($Z = 79$) and high electron density, GNPs exhibit greater attenuation and better contrast than iodine- and gadolinium-based agents [37–40]. Besides, GNPs are also inert, biocompatible, and have tunable surface characteristics by modifying with different ligands or polymers [12–14]. In addition, synthesis methods have advanced, allowing the control of the size and shape
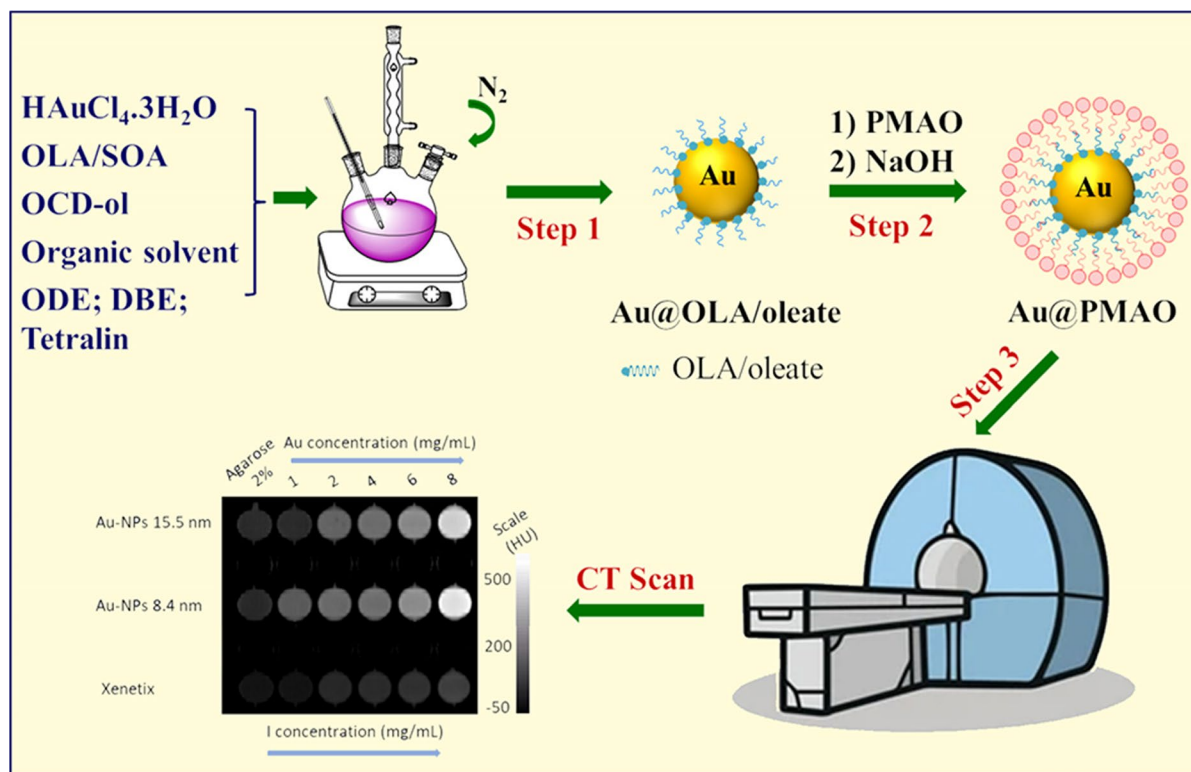
Scheme 1 Schematic synthesis of GNPs by thermal decomposition method and the ligand exchange process using PMAO

of GNPs. These features encourage using GNPs in biomedical imaging, especially CT imaging. The size of GNPs may affect their optical property, biocompatibility, and therapeutic utility [41, 42]. It has been reported that the size, shape, and concentration of GNPs influenced the cellular uptake as observed by cell monitoring applications [1, 36, 43]. On the other hand, the effect of these factors on the X-ray attenuation is currently contradictory [32, 44–48]. This work used the chemical reduction method to synthesize monodisperse Au nanoparticles of different sizes. The effect of the surfactants, oleylamine (OLA) and sodium oleate (SOA); solvent; and reaction time was investigated to determine the optimum conditions. The small-sized, uniform, and monodisperse GNPs were phase-transferred using poly(maleic anhydride-alt-1-octadecene) (PMAO) to be highly dispersive in aqueous solvent. In vitro CT imaging tests were carried out to evaluate the potential of the synthesized materials as CT contrast agents.

Experimental section

Materials

The main chemicals: gold (III) chloride hydrate (HAuCl$_4$.xH$_2$O, 99.99%), sodium oleate (SOA, 99%), oleylamine (OLA, 90%), 1-octadecanol (OCD-ol, 99%), 1-octadecene (ODE, 99%), 1,2,3,4-tetrahydro naphthalene (tetralin, 98%), dibenzyl ether (DBE, 99%), poly(maleic anhydride-alt-1-octadecene) (PMAO, 99%), absolute ethanol ($\geq$ 96%), hexane (99%), chloroform ($\geq$ 99%), and agarose were ordered from Sigma-Aldrich, Singapore. All chemicals were used as received without any purification.

Preparation

Synthesis of Au nanostructures: The GNPs colloidal property was fabricated by the 2-step procedure presented by Scheme 1.

In the first step, the GNPs were synthesized by chemical reduction in organic solvents. Herein, the precursor Au^{3+} was reduced by 1-octadecanol (OCD-ol) while oleylamine (OLA) or sodium oleate (SOA) both acted as complexing agents with Au^{3+} and surfactants. The as-synthesized GNPs were shielded by an OLA/oleate surfactant layer, thus unable to disperse in water. Therefore, the GNPs must be covered using poly(maleic anhydride-alt-octadecene) (PMAO), as shown in step 2.

First, $HAuCl_4.3H_2O$ and OLA (or SOA) at concentrations recorded in Table 1 were poured into a three-necked round bottom flask containing 40 mL of organic solvent (ODE, DBE, or tetralin). The reductant OCD-ol was added to the reaction mixture to reach a concentration of 90 mM. The reaction mixture was magnetically stirred under the nitrogen gas flow for 30 min at room temperature. Then, it was stirred at 80°C for 30 min. Finally, the reaction mixture was heated to 180°C gradually (at a speed of 5°C/min) and refluxed for 30–120 min. The collected products were left to cool down slowly to room temperature. The investigation parameters for the synthesis of GNPs are recorded in Table 1.

Following the fabrication, the GNPs were washed, and the procedure in our previous studies was mentioned [14]. For more details, a portion of the sample solution was mixed thoroughly with ethanol, and then centrifuged for 10 min at 10,000–12,000 rpm. After discarding the solvent, the precipitate was re-dispersed into n-hexane, and then re-precipitated again with ethanol. The washing process was repeated three to five times. The clean GNPs were characterized and saved for further investigation.

Transferring Au nanostructures into water   The GNPs, after synthesis in the organic solvent, were encapsulated by a layer of surfactants (OLA/oleate), thus dispersive in non-polar organic solvents. Surface modification by amphiphilic polymer PMAO helped them disperse in aqueous solution as follows:

One hundred and milligrams of the clean GNPs were poured into 2 mL of chloroform and ultrasonicated for 8–10 min until homogeneous. The obtained solution was denoted as solution 1.

Two grams of poly(maleic anhydrit-alt-1-octadecene) (PMAO) were dispersed into 20 mL of chloroform and ultrasonicated to obtain a homogeneous solution named solution 2.

Solution 1 was gradually added to solution 2, simultaneously ultra-sonicated; so, all GNPs were dispersed uniformly. The mixture was stirred at room temperature until chloroform completely evaporated. After that, 24 mL of NaOH 1M solution were added and magnetically stirred to get a homogeneous solution. The product was collected and washed with distilled water. When pH reached 7, the obtained GNPs were clean and able to disperse in aqueous medium.

Methods of characterization

Characterization of Au nanostructures   The crystal structures of the nanoparticles were characterized by powder XRD using Bruker D5005 X-ray diffractometer at room temperature with Cu Kα radiation ($\lambda = 1.5418$ Å). The morphological properties (physical size and shape) of the particles were obtained using transmission electron microscopy (TEM) on JEM-1010 (JEOL, Japan) operating at 50 kV and

Table 1 Surface plasmon resonance position of GNPs synthesized under different conditions

s	OLA (mM)	SOA (mM)	Slovents (mL)			Time (min)	Size (nm)	SPR (nm)
			ODE	DBE	Tetralin			
40	165	0	40	0	0	90	15.8 ± 0.9	522
	0	165					15.5 ± 0.8	522
40	0	165	40	0	0	90	15.5 ± 0.8	522
			0	40	0		12.8 ± 2.3	518
			0	0	40		14.3 ± 2.1	520
40	0	165	40	0	0	30	8.4 ± 0.6	516
						60	12.2 ± 0.7	518
						90	15.5 ± 0.8	522
						120	20.7 ± 3.2	531

high-resolution transmission electron microscope (HR-TEM) on JEM 2100 (JEOL, Japan). The infrared and UV–Vis spectra were obtained by the FT-IR NEXUS 670 (Nicolet, USA) and the UV–Vis spectrophotometer Jasco V-670 (Japan). The structures of materials were also studied by Fourier transform infrared (FT-IR) measurement using Nicolet iS10 (Thermo Scientific, USA) equipment. Dynamic light scattering (DLS) measurements of the magnetic fluids were examined by a Zetasizer (Malvern, UK). Inductively coupled plasma mass spectrometry was used to determine the amount of gold in the investigated samples on 7900 ICP-MS (Agilent, USA).

In vitro CT imaging studies   To assess the ability of a GNP's solution as a CT contrast agent, 2-mL wells containing GNPs solution at different concentrations (1, 2, 4, 6, and 8 mg/mL) were prepared. The testing wells were immobilized with 2% agarose gel by dissolving 2 g of agarose into 100 mL of distilled water at 80°C. The samples were left to cool down, solidified, and then put in a hand-made holder. To compare the X-ray attenuation coefficient, the commercial product Xenetix®300, which initially contained iodine at 300 mg/mL, was diluted to the same concentration with GNPs solutions. A 2% agarose solution

was used as the control in all experiments. The 128-Somatom Perspective CT scanner (Siemens, Germany) was used; the imaging parameters were as follows: source voltage of 120 kV and 80 mAs, slice thickness of 0.6 mm, display field of view (DFOV) x–y 278×295 mm^2, matrix size of 520×520. The CT images were loaded to a standard display program where a united region of interest (ROI) was selected to provide results for each sample. The increase in contrast was determined in the Houndfield unit (HU) by eFilm Workstation software (Merge Healthcare, USA).

Statistical analysis   The significance of the experimental data was assessed by one-way ANOVA with p-values of 0.05 and 0.01 that were considered significant.
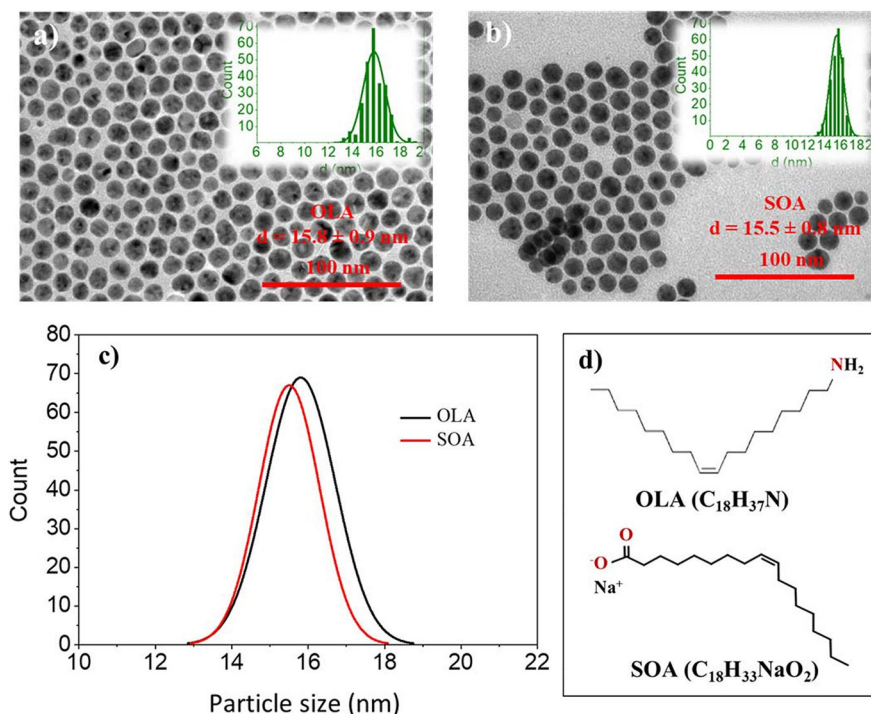
Results and discussion

The formation of Au nanostructures

Influence of surfactants on morphology

During the synthesis of GNPs, OLA/SOA acted as both complexing agents with Au^{3+} ions and

Fig. 1 The typical TEM images of Au nanostructures (**a**, **b**), physical size distribution curves (**c**), and surfactants (**d**) of GNPs synthesized in different surfactants

surfactants to avoid particle agglomeration. The effect of the surfactants OLA/SOA on the morphology of GNPs was analyzed by transmission electron microscopy, as presented in Fig. 1.

Morphology analysis of GNPs showed that the sample using OLA had a relatively uniform spherical shape with an average physical size from TEM measurements of 15.8 ± 0.9 nm (Fig. 1a). Using SOA led to the same result as OLA; the average size of spherical GNPs was 15.5 ± 0.8 nm (Fig. 1b). The size percentage errors in both cases were under 6%. It means there is no significant difference in particle shape, uniformity, and size (Fig. 1c) in both cases. This result is attributed to the structural similarity of OLA and SOA (Fig. 1d). During the synthesis, the nitrogen atom (NH_2 group) of the OLA molecule played the same role as the oxygen atom ($COO-$ group) of the oleate molecule, that is, electron donor to form dative covalent bonds with Au^{3+} and produce intermediate complexes. These complexes reacted with the reductant OCD-ol at high temperatures to form Au^0 atoms and Au crystal seeds. These seed crystals grow by diffusional deposition of Au atoms on existing seeds, and this indicates the formation of the Au nanoparticles. The crystal seeds grew by deposition of Au atoms on the existing seeds toward their diffusion, forming free Au nanoparticles. Since OLA/oleate was present in the reaction medium, they stuck to the surface of GNPs by donating their lone pairs on the N-tail (of OLA) or O-tail (of oleate) to the vacant orbitals of Au [49].

Hence, the utility of OLA and SOA produced monodisperse GNPs with excellent homogeneity. However, SOA is 3.5 times less expensive than OLA for the same quantity of usage. Consequently, SOA will reduce the production cost of GNPs. We used SOA in the following experiments to investigate other factors affecting the morphology and characteristics of the GNPs.

Influence of solvents on morphology

Previous papers have shown that solvent is one of the key figures during the formation and growth of crystal seeds [50]. Our work aimed to study the effect of different solvents, such as ODE, BDE, and tetralin, on the morphology and size of GNPs. The TEM analysis is demonstrated in Fig. 2.

As can be seen, the gold nanoparticles (GNPs) formed in ODE solvent were monodisperse, spherical, and relatively uniform with an average size of 15.5 ± 0.8 nm; the size distribution was narrow with a fairly small size percentage error ($>5.2\%$) (Fig. 2a). The sample produced in DBE solvent also had a spherical shape with a clear grain boundary but lower uniformity. In this solvent, the average size was 12.8 ± 2.3 nm, and the size error reached approximately 18% (Fig. 2b). Tetralin solvent led to the formation of uneven GNPs: some particles agglomerated, and the average size was 14.3 ± 2.1 nm with a size percentage error of up to 14.7% (Fig. 2c). Accordingly, all three solvents produced spherical NPs with a size ranging from 12.8 to 15.5 nm (Fig. 2d). The uniformity depended on the type of solvent. ODE facilitated the formation of uniform and monodisperse GNPs with narrow size distribution. The solvents DBE and tetralin resulted in less uniform NPs with wider size distribution. This observation can be explained based on the structure of solvents. In particular, ODE has an unbranched carbon chain, similar to SOA, while BDE and tetralin contain spatially cumbersome carbon rings. The steric hindrance undoubtedly impacts the formation and growth of crystal seeds into the Au materials. For this reason, ODE solvent was chosen for further investigation.

Influence of time on the morphology

Along with the reagents directly participating in the morphology development and size of GNPs, the reaction time also matters. The dependence of morphology on reaction time ranging from 30 to 120 min was examined by TEM, as shown in Fig. 3.

The TEM images of GNPs indicated that the reaction time varied in the 30–120-min range. All the obtained GNPs had spherical shapes; however, their size distribution and uniformity changed obviously. At $t = 30$, 60, and 90 min (Fig. 3a–c), the collected GNPs were spherical, monodisperse, and relatively uniform with an average size of 8.4 ± 0.6 nm, 12.2 ± 0.7 nm, and 15.5 ± 0.8 nm, respectively. The size distribution of these samples was comparatively narrow (Fig. 3e), with size percentage errors all under 8%. The resultant particles became uneven as the reaction time was prolonged to 120 min. In addition to gold nanospheres, some GNPs overlapped to

Fig. 2 TEM images (**a**, **b**, **c**) and corresponding physical size distribution histograms (**d**) of GNPs synthesized in different solvents
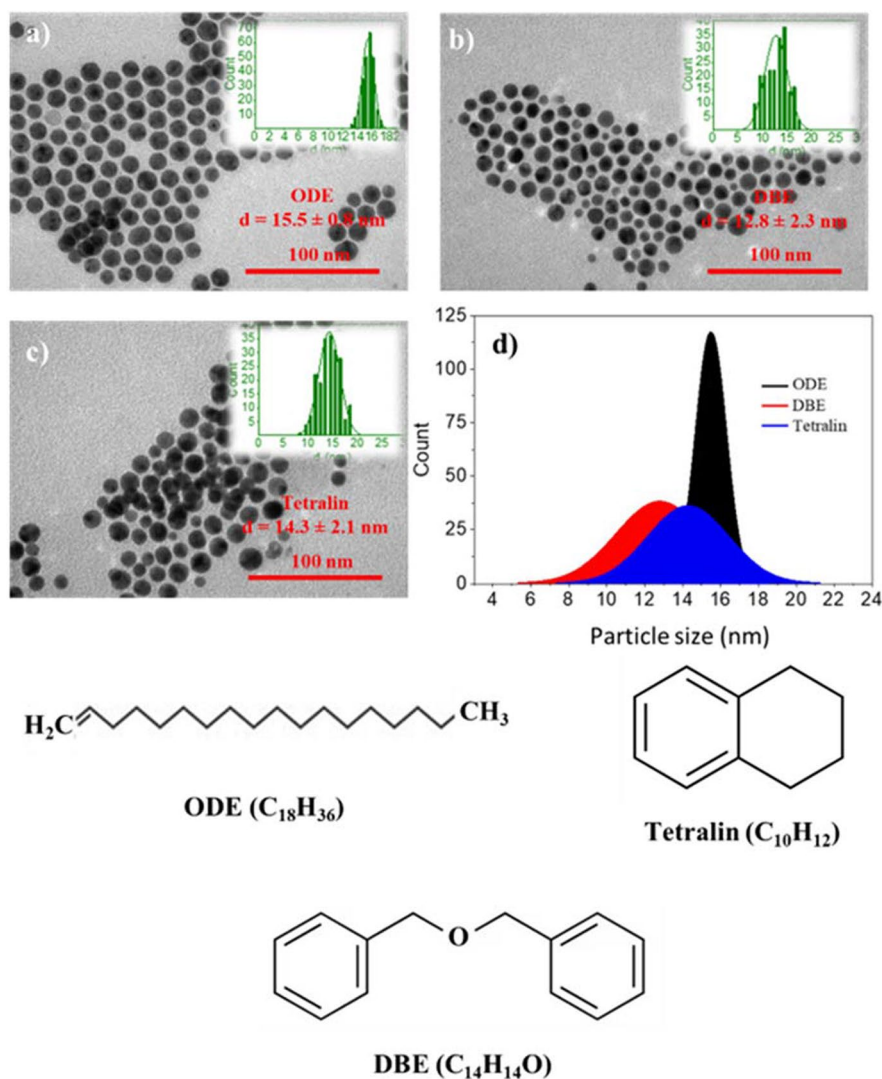
form different shapes (Fig. 3d) with increasing size. The average size in this instance rose to 20.7 ± 3.2 nm with a particle size error of 15.4%. To put it briefly, the average particle size increases from 8.4 to 20.7 nm, corresponding to the increasing reaction time from 30 to 120 min. A plausible explanation for this observation is that the total surface energy forces the particles in the reaction system to agglomerate. Thus, the average size of GNPs enlarges [51]. As such, the size of GNPs can be controlled by adjusting the reaction time.

A presentative Au sample, synthesized in 90 min, was analyzed by HR-TEM with a magnification of 600,000 times (Fig. 4a). The HR-TEM image showed

that the size of GNPs was 15.7 nm, equivalent to the size observed by TEM (Fig. 3c). Selected area electron diffraction (SEAD) analysis of a single gold particle is demonstrated in Fig. 4b. As observed, the SEAD of the GNPs included four concentric circles, which were assigned to the planes (111), (200), (220), and (311) of the face-centered cubic (fcc) crystal. It is suggested that the as-fabricated GNPs have high crystallinity [52].

Deduced from the above investigation, synthesis in ODE solvent using SOA as a surfactant with a 30–90-min reaction time provided GNPs owning high uniformity, mono dispersion, and small size (8.4–15.5 nm), appropriate for biomedical purposes.
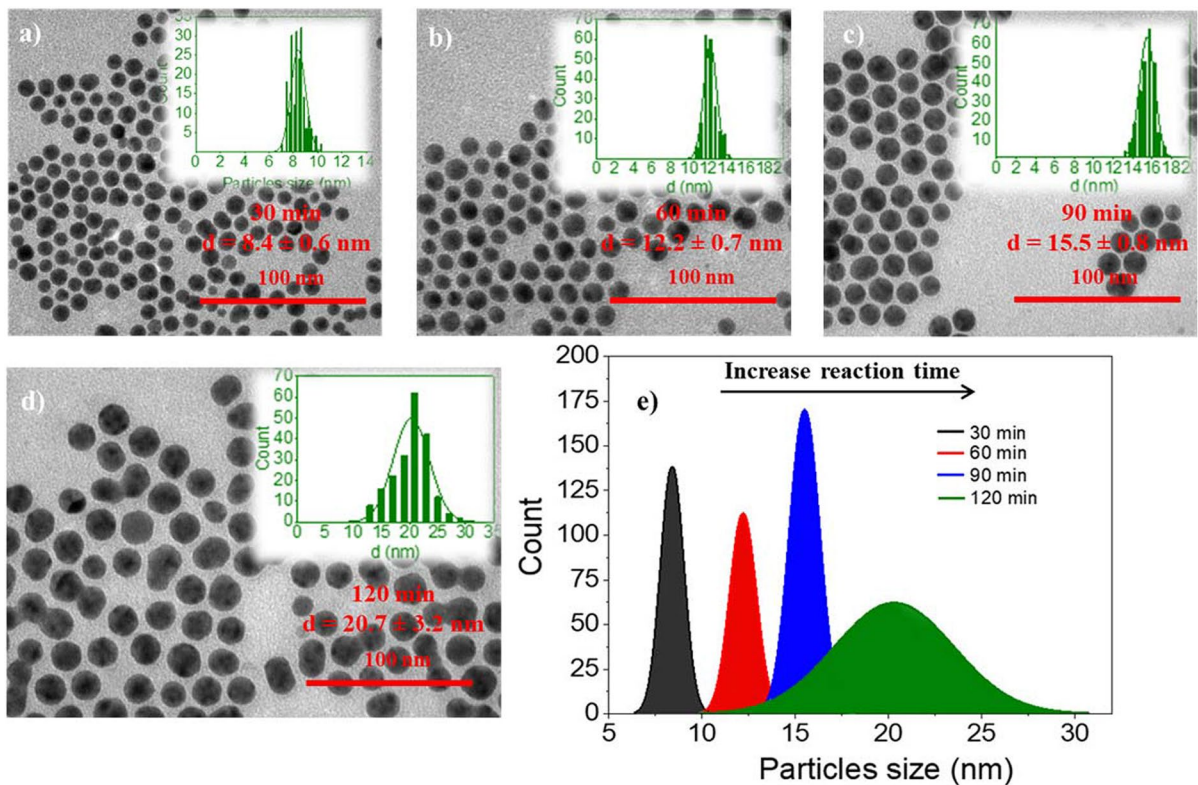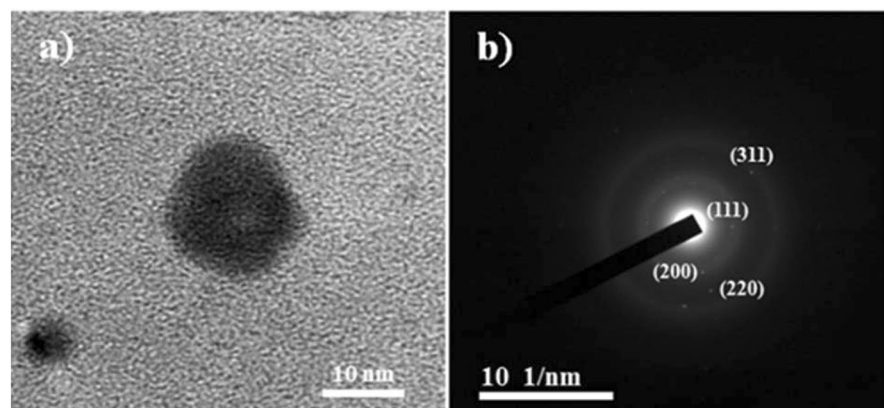
Fig. 3 TEM images (**a**, **b**, **c**, **d**), and corresponding physical size distribution histograms (**e**) of GNPs synthesized at different times

Fig. 4 HR-TEM images (**a**) and SEAD images (**b**) of GNPs

Optical properties

The influence of reaction parameters on the optical properties of the as-synthesized GNPs is illustrated in Table 1 and Fig. 5.

The surface plasmon resonance (SPR) position of all GNPs fabricated using OLA and SOA was 522 nm with similar intensity and width of peaks (Fig. 5a).

The same observation is obtained when comparing their average particle size (Table 1).

The maximum absorption peaks of samples formed in ODE, tetralin, and DBE were at 522, 520, and 518 nm, respectively (Fig. 5b). The variation of the maximum absorption peak is due to the size of GNPs in solvents ODE, tetralin, and DBE decreasing from 15.5 ± 0.8, 14.3 ± 2.1, and 12.8 ± 2.3 nm.
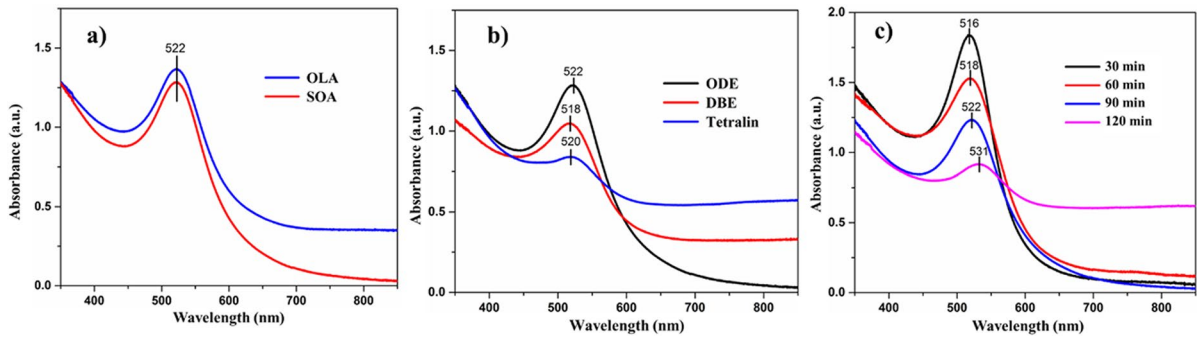
Fig. 5 UV–Vis of GNPs fabricated by different surfactants (**a**), solvents (**b**), and time (**c**)

Compared to the absorption peaks of GNPs formed in ODE solvent, those of samples produced in tetralin and DBE were expanded. However, the expansion of the two samples was not equivalent. As mentioned, some GNPs in tetralin solvent were overlapped, causing agglomeration (TEM image, Fig. 2). According to Mie's theory, the maximum absorption peak of optical NPs depends on their size and shape. That is, our results agree with Mie's theory [53].

As reaction time varied from 30 to 120 min, the maximum SPR absorption peak shifted from 516 to 531 nm (Fig. 7). The GNPs synthesized in 30–90 min exhibited narrow peaks since they were uniformly spherical with a small size (8.4–15.5 nm). Meanwhile, the GNPs obtained after 120 min had widened absorption peaks due to the larger size and the overlap of GNPs, distorting their original shape. The shift and expansion of the absorption peak of GNPs toward the longer wavelengths were caused by the increased

size. It is shown in Fig. 2 that the larger the size, the longer the maximum absorption peak value.

This evidence indicated that under the reaction conditions, the average size of GNPs changed from 8.4 to 20.7 nm, corresponding to the SPR absorption peaks at 516–531 nm (Table 1). Thus, we chose two GNPs samples with the average size of 8.4 and 15.5 nm for the following steps.

The crystal phase of GNPs

To examine the degree of crystallinity of the as-fabricated GNPs, X-ray diffraction (XRD) patterns of two representative GNPs with an average size of 8.4 ± 0.6 and 15.5 ± 0.8 nm, denoted as Au-8.4 and Au-15.5, were recorded. The 2θ ranged from $20°$ to $70°$. The result is demonstrated in Fig. 6a.

Both representative GNPs showed sharp diffraction peaks with high intensity at $2\theta = 38.27°$, $44.49°$, and $64.69°$, corresponding to the characteristic planes (111), (200), and (220) of the fcc structure of Au

Fig. 6 XRD patterns of GNPs at different sizes (**a**) and FT-IR spectra of polymer, OA/OLA, and PMAO encapsulated GNPs (**b**)
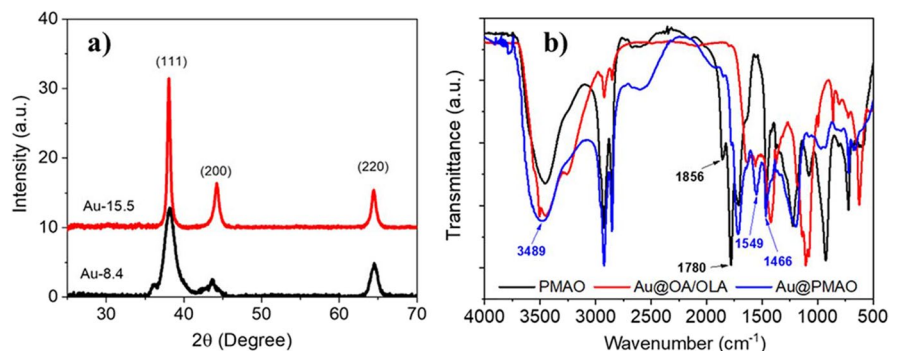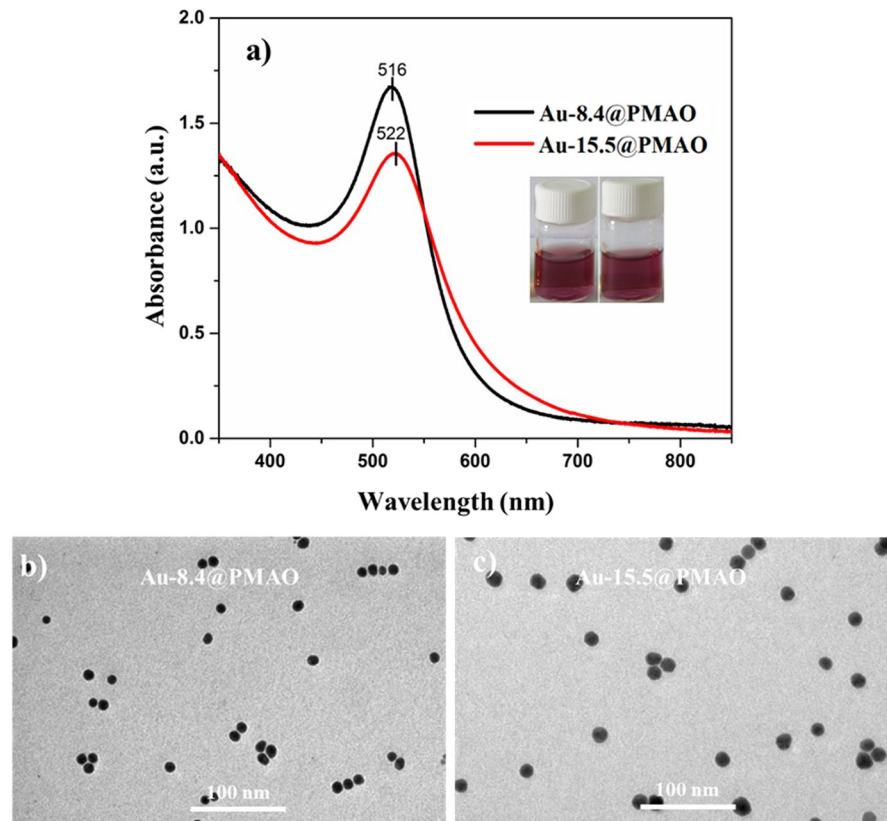
Fig. 7 Images of solutions (**a**) and the UV–Vis spectra (**b**) of GNPs with different sizes after PMAO, encapsulation dispersed in water

(JCPDS, 01—1172) [54]. This result is consistent with SEAD information as presented in Fig. 4b. We identified lattice parameter (Fig. 4a) from XRD patterns for both Au-8.4 and Au-15.5 samples, that is, 0.4061 and 0.4053 nm, respectively. Our obtained values are concordant with previous reports [55]. The XRD peaks of the Au-8.4 sample were wider than those of the Au-15.5 sample, as expected since the average size of the Au-8.4 sample was smaller than the Au-15.5 sample. From the half-width at the (111) maximum peak, the average size of GNPs can be calculated by the Debye–Scherrer equation. The values corresponding to the samples Au-8.4 and Au-15.5 were 8.2 and 15.3 nm, respectively.

Using the polymer PMAO as an encapsulating agent helped increase the biocompatibility of the materials. The formation of PMAO coating on the nanoparticle surface after phase transfer was examined by Fourier transform infrared (FT-IR) (Fig. 6b). We can see that the two peaks at 1856 and 1780 cm^{-1} in IR spectrum of PMAO due to vibrations of the anhydride ring are absent in the IR spectrum of

Au@PMAO, but two new peaks at 1549 and 1466 cm^{-1} in this spectrum showed that anhydride ring is opened and changed to be COO^- groups. Two new peaks were attributed to the symmetry and asymmetry vibration of the carboxylate group of PMAO in the IR spectrum of Au@PMAO. Moreover, the nanoparticles after phase transfer (Au@PMAO) gave a broad maximum absorption range at a wave number of 3489 cm^{-1} that was assigned to the vibration of OH in water molecules absorbed onto PMAO coating. These changes in IR spectra confirmed the presence of PMAO coating layer on the surface of Au nanoparticles.

Particle size and stability of the PMAO-coated Au NPs

The images of PMAO-modified GNPs solution are presented in Fig. 7a. As can be seen, both solutions were homogeneous without sedimentation. The UV–Vis spectra proved that the optical properties of both samples did not change after encapsulation by
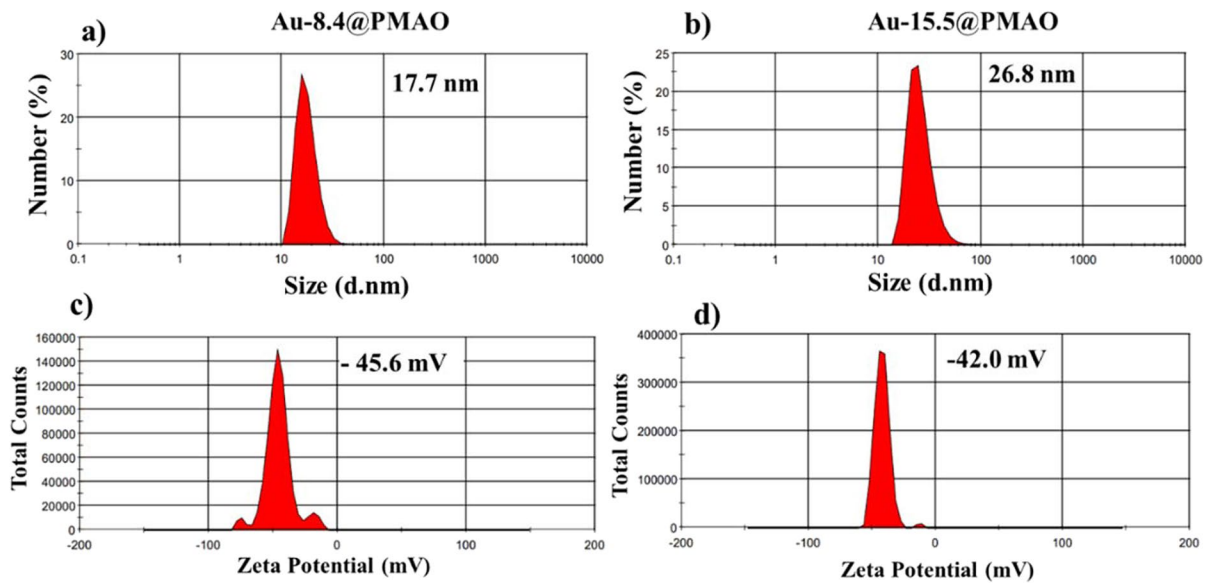
Fig. 8 DLS hydrodynamic diameters (**a**, **b**) and zeta potentials (**c**, **d**) of the samples Au-8.4@PMAO (**a**, **c**) and Au-15.5@PMAO (**b**, **d**) dispersed in water

PMAO. Their maximum absorption peaks appear at 516 and 522 nm, corresponding to the samples Au-8.4@PMAO and Au-15.5@PMAO (Fig. 7a).

As observed in TEM images, the PMAO-modified GNPs (Fig. 7b and c) were monodisperse; no particle agglomeration occurred. The size of two samples, Au-8.4@PMAO and Au-15.5@PMAO, was close to that of the original GNPs. However, the DLS diameters of Au-8.4@PMAO and Au-15.5@PMAO were correspondingly 17.7 and 26.8 nm (Fig. 8a, b), higher than the values estimated from TEM. It is reasonable since the DLS technique allows the measure of the coverage of PMAO.

The stability of GNPs after encapsulation by PMAO was evaluated by measuring zeta potential (Fig. 8c and d). The zeta potential of aqueous Au-8,4@PMAO and Au-15.5@PMAO solutions were − 45.6 and − 42.0 mV. The colloidal suspensions with a zeta potential in the range of 40–60 mV are considered stable [56]. Hence, the PMAO-encapsulated GNPs were relatively stable in aqueous medium, suitable for application in biomedicine.

Contrast enhancement in vitro CT imaging

Using gold nanoparticles (GNPs) solution as a CT imaging contrast agent is preferable to the standard iodine-based compounds due to the X-ray attenuation [57]. To better understand the efficiency of GNPs as CT contrast agents, solutions of Au-8.4@PMAO and Au-15.5@PMAO at different concentrations were tested and collated with the agarose 2% solution as the control. Moreover, we also used the commercial contrast agent Xenetix (containing iodine) at equivalent concentrations to compare the X-ray attenuation intensity. CT images were analyzed using the efilm workstations program (Merge Healthcare, USA) based on the signal intensity in the HU. Figure 9 shows the CT images using the GNPs and commercial Xenetix at different Au and I concentrations, the corresponding HU values, and X-ray attenuation intensity.

The increase in the X-ray attenuation intensity from low to high concentrations of Au-8.4@PMAO, Au-15.5@PMAO, and Xenetix can be observed, as shown in Fig. 9a. When the concentration of samples varied from 1 to 8 mg/mL, the CT contrast intensity of all rose linearly (Fig. 9b), corresponding to the increase of HU values (Fig. 9c). As expected, the correlation between the CT imaging contrast and the concentration of Au and I was linear, according to the average greyscale range. The R^2 values obtained
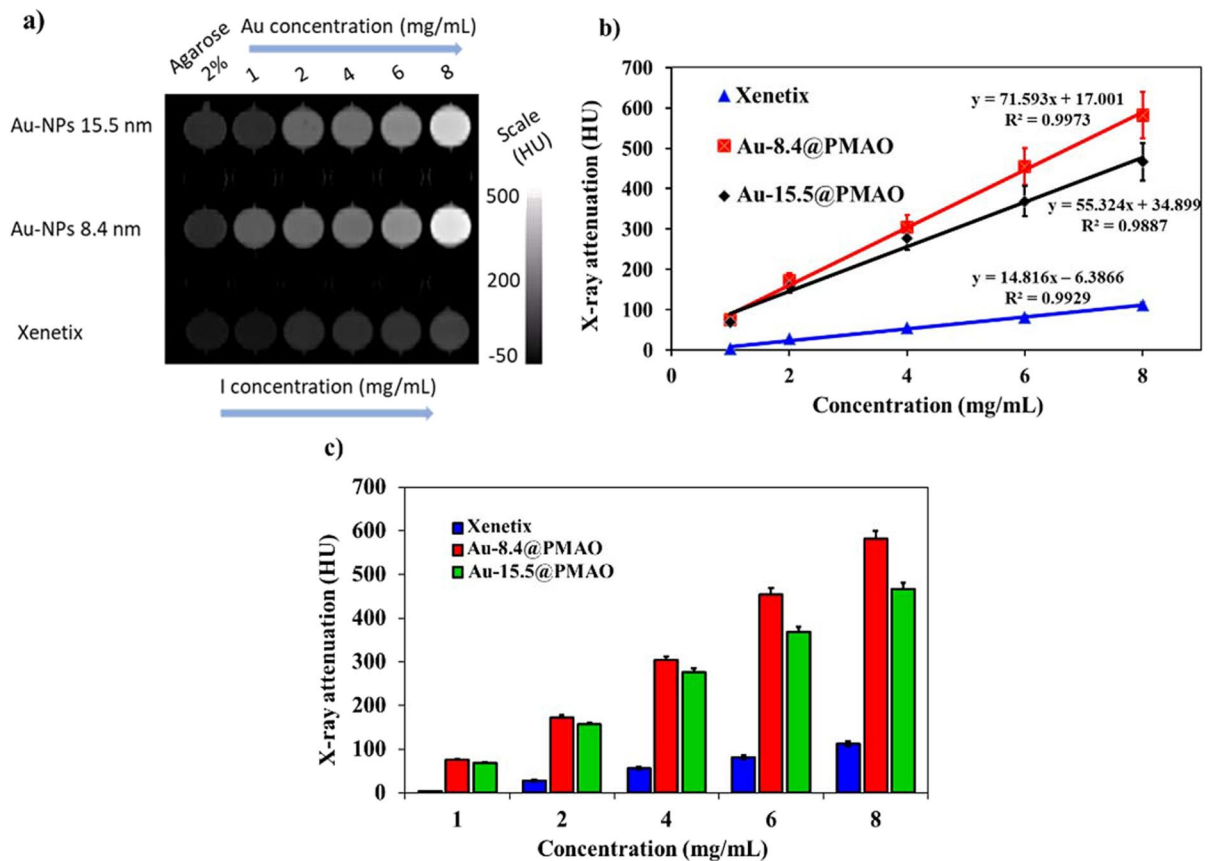
Fig. 9 CT images of the nano Au-8.4@PMAO, nano Au-15.5@PMAO, and Xenetix at different concentrations (**a**), the corresponding linear plots of X-ray attenuation vs. concentrations (**b**) and HU values of samples at equivalent concentrations (**c**)

from Au-8.4@PMAO, Au-15.5@PMAO, and Xenitex were 0.9973, 0.9887, and 0.9929, respectively (Fig. 9b).

Figure 9a indicates the statistically significant difference ($P < 0.05$) in X-ray attenuation between the gold nanoparticles (GNPs) samples and the commercial Xenetix. The GNPs samples exhibited the outstanding capability to attenuate X-radiation compared to Xenetix. At the investigated concentration of 2 mg/mL, the HU intensities of Au-8.4@PMAO and Au-15.5@PMAO were 6.2 and 5.6 times higher than that of the commercial Xenetix (Fig. 9c). This result fits the X-ray attenuation property of the contrast agent Omnipaque and nano gold in other studies [26, 58–60]. According to the work of Tingting Xiao et al. to reach the equivalent HU signal of our GNPs, the concentrations of nano gold and iodine (in Omnipaque) must be much higher [61]. Therefore,

this study has confirmed that the X-ray attenuation intensity of our GNPs was significantly higher than the commercial products, such as Omnipaque and Xenetix. It makes sense because, theoretically, the attenuation ability of Au is 2.7 times higher than iodine. At 100 keV, the values of Au and iodine are 5.16 and 1.94 cm^2/g, respectively, corresponding to the higher atomic number of Au (Z=79) than that of I (Z=53) [4]. Due to the remarkable X-ray attenuation of our Au material compared with the iodine complexes and its low toxicity at investigated concentrations compared to zirconium dioxide and barium sulfate [62], we propose GNPs as a promising CT contrast alternative.

Figure 9a also visualizes the statistically significant difference ($P < 0.01$) in X-ray attenuation between two GNPs samples: Au-8.4@PMAO and Au-15.5@PMAO. The distinction suggested

the effect of particle size on the X-ray attenuation intensity. At the same concentration of GNPs, the smaller particle sample (Au-8.4@PMAO) displayed a greater attenuation than the larger one (Au-15.5@ PMAO). Consequently, the small-sized GNPs would be a more effective CT contrast agent. Nevertheless, in practice, the attenuation effect of GNPs at low concentrations is hard to detect. In this study, at the concentration of 1 mg/mL, there was a negligible attenuation difference between two GNPs samples with TEM sizes of 8.4 and 15.5 nm. The difference became obvious as the concentration increased to 2 mg/mL. Particularly, the X-ray attenuation of GNPs 8.4 nm in the HU unit was approximately 10% higher than that of GNPs 15.5 nm. The distinction rose to around 25% at the concentration of 8 mg/mL (Fig. 9c). Reasonably, the surface area increases as the size of particles decreases [63]. These results are consistent with studies of Sun et al. [32]. Our investigation intimated the potential of the synthesized GNPs as a CT imaging contrast agent.

Conclusion

We successfully fabricated the spherical, monodisperse, and uniform GNPs in organic solvents. Investigation of synthesis conditions revealed the similar influence of OLA and SOA as surfactants on the morphology and uniformity of particles. The solvent ODE and reaction time varying from 30 to 60 min facilitated the formation of the uniform and monodisperse GNPs. Characterization showed that the fabricated GNPs were crystalline and spherical with a fcc structure and an average size of 8.4–20.7 nm, with maximum SPR peaks in the 516–531-nm range. After the surface modification by PMAO, the GNPs were highly stable in the aqueous solution with the zeta potential of -45.6 and -42 mV, hydrodynamic diameter of 17.7 and 26.8 nm, corresponding to the samples 8.4 and 15.5 nm. In vitro CT imaging test expressed the notable capability of GNPs as a contrast agent. The smaller GNPs exhibited higher attenuation than the larger ones. As the concentration of Au rose from 1 to 8 mg/mL, the CT contrast increased. The CT contrast signal of the nano Au@PMAO was higher than that of the commercial Xenetix at the same testing concentration.

With these excellent properties, the Au@PMAO synthesized in this study proved a promising candidate for CT imaging in practice.

Declarations

References

1. Chithrani BD, Ghazani AA, Chan WCW (2006) Determining the size and shape dependence of gold nanoparticle uptake into mammalian cells. Nano Lett 6:662–668. https://doi.org/10.1021/nl052396o
2. Kircher MF, Willmann JK (2012) Molecular body imaging: MR imaging, CT, and US. Part I Principles Radiology 263:633–643. https://doi.org/10.1148/radiol.12102394
3. Pelc NJ (2014) Recent and future directions in CT imaging. Ann Biomed Eng 42:260–268. https://doi.org/10.1007/s10439-014-0974-z
4. Reuveni T, Motiei M, Romman Z, Popovtzer A, Popovtzer R (2011) Targeted gold nanoparticles enable molecular CT imaging of cancer: an in vivo study. Int J Nanomedicine 6:2859–2864. https://doi.org/10.2147/ijn.s25446
5. Lusic H, Grinstaff MW (2013) X-ray-computed tomography contrast agents. Chem Rev 113:1641–1666. https://doi.org/10.1021/cr200358s
6. Bernstein AL, Dhanantwari A, Jurcova M, Cheheltani R, Naha PC, Ivanc T, Shefer E, Cormode DP (2016) Improved sensitivity of computed tomography towards iodine and gold nanoparticle contrast agents via iterative reconstruction methods. Sci Rep 6:1–9. https://doi.org/10.1038/srep26177
7. Cormode DP, Naha PC, Fayad ZA (2014) Nanoparticle contrast agents for computed tomography: a focus on micelles. Contrast Media Mol Imaging 9:37–52. https://doi.org/10.1002/cmmi.1551
8. Ashton JR, West JL, Badea CT (2015) In vivo small animal micro-CT using nanoparticle contrast agents. Front Pharmacol 6:1–22. https://doi.org/10.3389/fphar.2015.00256
9. Ghann WE, Aras O, Fleiter T, Daniel MC (2012) Syntheses and characterization of lisinopril-coated gold nanoparticles as highly stable targeted CT contrast agents in cardiovascular diseases. Langmuir 28:10398–10408. https://doi.org/10.1021/la301694q
10. Boote E, Fent G, Kattumuri V, Casteel S, Katti K, Chanda N, Kannan R, Katti K, Churchill R (2010) Gold

nanoparticle contrast in a phantom and juvenile swine. Acad Radiol 17:410–417. https://doi.org/10.1016/j.acra.2010.01.006

11. Shilo M, Reuveni T, Motiei M, Popovtzer R (2012) Nanoparticles as computed tomography contrast agents: current status and future perspectives". Nanomedicine 7:257–269. https://doi.org/10.2217/nnm.11.190

12. Daniel MC, Astruc D (2004) Gold nanoparticles: assembly, supramolecular chemistry, quantum-size-related properties, and applications toward biology. Catalysis, and Nanotechnology. Chem Rev 104:293–346. https://doi.org/10.1021/cr030698+

13. Naha PC, Chhour P, Cormode DP (2015) Systematic in vitro toxicological screening of gold nanoparticles designed for nanomedicine applications. Toxicol Vitr 29:1445–1453. https://doi.org/10.1016/j.tiv.2015.05.022

14. Dung NT, Linh NTN, Chi DL, Hoa NTH, Hung NP, Ha NT, Nam PH, Phuc NX, Tam LT, Le TLu (2021) Optical properties and stability of small hollow gold nanoparticles. RSC Adv 11:13458–13465. https://doi.org/10.1039/d0ra09417j

15. Rabin O, Perez JM, Grimm J, Wojtkiewicz G, Weissleder R (2006) An X-ray computed tomography imaging agent based on long-circulating bismuth sulphide nanoparticles. Nat Mater 5:118–122. https://doi.org/10.1038/nmat1571

16. Yu SB, Watson AD (1999) Metal-based X-ray contrast media. Chem Rev 99:2353–2377. https://doi.org/10.1021/cr980441p

17. Pannu HK, Thompson RE, Phelps J, Magee CA, Fishman EK (2005) Optimal contrast agents for vascular imaging on computed tomography: iodixanol versus iohexol. Acad Radiol 12:576–584. https://doi.org/10.1016/j.acra.2005.01.015

18. Voert CEM, Kour RYN, Teeffelen BCJ, Ansari N, Stok KS (2020) Contrast-enhanced micro-computed tomography of articular cartilage morphology with ioversol and iomeprol. J Anat 237:1062–1071. https://doi.org/10.1111/joa.13271

19. Oliva MR, Erturk SM, Ichikawa T, Rocha T, Ros PR, Silverman SG, Mortele KJ (2012) Gastrointestinal tract wall visualization and distention during abdominal and pelvic multidetector ct with a neutral barium sulphate suspension: comparison with positive barium sulphate suspension and with water. JBR–BTR. 95, 237–242. https://doi.org/10.5334/jbr-btr.628

20. Cormode DP, Jarzyna PA, Mulder WJM, Fayad ZA (2012) Modified natural nanoparticles as contrast agents for medical imaging. Adv Drug Deliv Rev 62:329–338. https://doi.org/10.1016/j.addr.2009.11.005

21. Hsu JC, Nieves LM, Betzer O, Sadan T, Noël PB, Popovtzer R, Cormode DP (2021) Nanoparticle contrast agents for X-ray imaging applications. Wiley Interdiscip Rev Nanomed Nanobiotechnol 12(6):e1642. https://doi.org/10.1002/wnan.1642.Nanoparticle

22. Cochran ST (2005) Anaphylactoid reactions to radiocontrast media Curr. Allergy Asthma Rep 5:28–31. https://doi.org/10.1007/s11882-005-0051-7

23. Mruk B (2016) Renal safety of iodinated contrast media depending on their osmolarity - current outlooks. Polish J Radiol 81:157–165. https://doi.org/10.12659/PJR.895406

24. Hainfeld JF, Slatkin DN, Focella TM, Smilowitz HM (2006) Gold nanoparticles: a new X-ray contrast agent. Br J Radiol 79:248–253. https://doi.org/10.1259/bjr/13169882

25. Cormode DP, Cormode DP, Skajaa T, Schooneveld MM, Koole R, Jarzyna P, Lobatto ME, Calcagno C, Barazza A, Gordon RE, Zanzonico P, Fisher EA, Fayad ZA, Mulder WJM (2008) Nanocrystal core high-density lipoproteins-a multimodality contrast agent platform. Nano. Lett. 8:3715–3723. https://doi.org/10.1021/nl801958b

26. Peng C, Zheng L, Chen Q, Shen M, Guo R, Wang H, Cao X, Zhang G, Shi X (2012) PEGylated dendrimer-entrapped gold nanoparticles for in vivo blood pool and tumor imaging by computed tomography. Biomaterials 33:1107–1119. https://doi.org/10.1016/j.biomaterials.2011.10.052

27. Jackson PA, Rahman WNWA, Wong CJ, Ackerly T, Geso M (2010) Potential dependent superiority of gold nanoparticles in comparison to iodinated contrast agents. Eur J Radiol 75:104–109. https://doi.org/10.1016/j.ejrad.2009.03.057

28. Lee DE, Koo H, Sun IC, Ryu JH, Kim K, Kwon IC (2012) Multifunctional nanoparticles for multimodal imaging and theragnosis. Chem Soc Rev 41:2656–2672. https://doi.org/10.1039/c2cs15261d

29. Cai QY, Kim SH, Choi KS, Kim SY, Byun SJ, Kim KW, Park SH, Juhng SK, Yoon KH (2007) Colloidal gold nanoparticles as a blood-pool contrast agent for x-ray computed tomography in mice. Invest Radiol 42:797–806. https://doi.org/10.1097/RLI.0b013e31811ecdcd

30. Moghimi SM, Hunter AC, Murray JC (2014) Long-circulating and target-specific nanoparticles : theory to practice. Pharmacol Rev. 2001, 53, 283–318. https://www.researchgate.net/publication/11980988_Long-Circulating_and_Target-Specific_Nanoparticles_Theory_to_Practice

31. Eck W, Nicholson AI, Zentgraf H, Semmler W, Bartling S (2010) Anti-CD4-targeted gold nanoparticles induce specific contrast enhancement of peripheral lymph nodes in X-ray computed tomography of live mice. Nano Lett 10:2318–2322. https://doi.org/10.1021/nl101019s

32. Chenjie X, Tung GA, Shouheng S (2008) Size and concentration effect of gold nanoparticles on X-ray attenuation as measured on computed tomography. Chem Mater 20:4167–4169. https://doi.org/10.1021/cm8008418

33. Fang Y, Peng C, Guo R, Zheng L, Qin J, Zhou B, Shen M, Lu X, Zhang G, Shi X (2013) Dendrimer-stabilized bismuth sulfide nanoparticles: synthesis, characterization, and potential computed tomography imaging applications. Analyst 138:3172–3180. https://doi.org/10.1039/c3an00237c

34. Xiao YD, Paudel R, Liu J, Ma C, Zhang ZS, Zhou SK (2016) MRI contrast agents: classification and application (Review). Int J Mol Med 38:1319–1326. https://doi.org/10.3892/ijmm.2016.2744

35. Thomsen HS (2006) Nephrogenic systemic fibrosis: a serious late adverse reaction to gadodiamide.

Eur Radiol 16:2619–2621. https://doi.org/10.1007/s00330-006-0495-8

36. Hajfathalian M, Amirshaghaghi A, Naha PC, Chhour P, Hsu JC, Douglas K, Dong Y, Sehgal CM, Tsourkas A, Neretina S, Cormode DP (2018) Wulff in a cage gold nanoparticles as contrast agents for computed tomography and photoacoustic imaging. Nanoscale 10:18749–18757. https://doi.org/10.1039/c8nr05203d

37. Cole LE, Ross RD, Tilley JM, Vargo-Gogola T, Roeder RK (2015) Gold nanoparticles as contrast agents in X-ray imaging and computed tomography. Nanomedicine 10:321–341. https://doi.org/10.2217/nnm.14.171

38. Oumano M, Russell L, Salehjahromi M, Shanshan L, Sinha N, Ngwa W, Yu H (2021) CT imaging of gold nanoparticles in a human-sized phantom. J Appl Clin Med Phys 22:337–342. https://doi.org/10.1002/acm2.13155

39. Mieszawska AJ, Mulder WJM, Fayad ZA, Cormode DP (2013). Mol. Pharmaceutics. 10, 831–847

40. Kiessling F, Pichler BJ, Hauff P (2017) Small animal imaging. Springer Cham. https://doi.org/10.1007/978-3-319-42202-2

41. Haiss W, Thanh NTK, Aveyard J, Fernig DG (2007) Determination of size and concentration of gold nanoparticles from UV-Vis spectra. Anal Chem 79:4215–4221. https://doi.org/10.1021/ac0702084

42. Dong YC, Hajfathalian M, Maidment PSN, Hsu JC, Naha PC, Si-Mohamed S, Breuilly M, Kim J, Chhour P, Douek P, Litt HI, Cormode DP (2019) Effect of gold nanoparticle size on their properties as contrast agents for computed tomography. Sci. Rep. 9:14912. https://doi.org/10.1038/s41598-019-50332-8

43. Chhour P, Kim J, Benardo B, Tovar A, Mian S, Litt HI, Ferrari VA, Cormode DP (2017) Effect of gold nanoparticle size and coating on labeling monocytes for CT tracking. Bioconjugate Chem 28:260–269. https://doi.org/10.1021/acs.bioconjchem.6b00566

44. Khademi S, Sarkara S, Kharrazid S, Aminie SM, Zadehf AS, Ay MR, Ghadiri H (2017) Evaluation of size, morphology, concentration, and surface effect of gold nanoparticles on X-ray attenuation in computed tomography. Phys Medica 45:127–133. https://doi.org/10.1016/j.ejmp.2017.12.001

45. Y Dou Y Guo X Li X Li S Wang L Wang G Lv X Zhang H Wang X Gong and, 2016 J Chang Size-tuning ionization to optimize gold nanoparticles for simultaneous enhanced CT imaging and radiotherapy ACS Nano 10 2536 2548 https://doi.org/10.1021/acsnano.5b07473

46. Ross RD, Cole LE, Tilley JMR, Roeder RK (2014) Effects of functionalized gold nanoparticle size on X-ray attenuation and substrate binding affinity. Chem Mater 26:1187–1194. https://doi.org/10.1021/cm4035616

47. Hirn S, Behnke MS, Schleh C, Wenk A, Lipka J, Schäffler M, Takenaka S, Möller W, Schmid G, Simon U, Kreyling WG (2011) Particle size-dependent and surface charge-dependent biodistribution of gold nanoparticles after intravenous administration. Eur J Pharm Biopharm 77:407–416. https://doi.org/10.1016/j.ejpb.2010.12.029

48. Takeuchi I, Nobata S, Oiri N, Tomoda K, Makino K (2017) Biodistribution and excretion of colloidal gold nanoparticles after intravenous injection: effects of particle size. Biomed Mater Eng 28:315–323. https://doi.org/10.3233/BME-171677

49. Fratoddi I, Venditti I, Cametti C, Russo MV (2017) Gold nanoparticles and gold nanoparticle-conjugates for delivery of therapeutic molecules. Progress and challenges. J Mater Chem B 2:4204–4220. https://doi.org/10.1039/c4tb00383g

50. Lu LT, Dung NT, Tung LD, Thanh CT, Quy OK, Chuc NV, Maenosono S, Thanh NTK (2015) Synthesis of magnetic cobalt ferrite nanoparticles with controlled morphology, monodispersity and composition: the influence of solvent, surfactant, reductant and synthetic conditions. Nanoscale 7:19596–19610. https://doi.org/10.1039/c5nr04266f

51. Yamashita Y, Miyahara R, Sakamoto K (2017) Emulsion and emulsification technology. Elsevier Inc. Chapter 28, 489–506. https://doi.org/10.1016/B978-0-12-802005-0.00028-8

52. Fodjo EK, Canlier A, Kong C, Yurtsever A, Guillaume PL, Patrice FT, Abe M, Tohei T, Sakai A (2018) Facile synthesis route of Au-Ag nanostructures soaked in PEG. Adv Nanoparticles 7:37–45. https://doi.org/10.4236/anp.2018.72004

53. Novak JP, Feldheim DL (2000) Assembly of phenylacetylene-bridged silver and gold nanoparticle arrays. JACS 122:3979–3980. https://doi.org/10.1021/ja000477a

54. Kalyan Kamal SS, Vimala J, Sahoo PK, Ghosal P, Ram S, Durai L (2014) A green chemical approach for synthesis of shape anisotropic gold nanoparticles. Int Nano Lett 4:109–115. https://doi.org/10.1007/s40089-014-0109-4

55. Ha Pham TT, Dien ND, Vu XH (2021) Facile synthesis of silver/gold alloy nanoparticles for ultra-sensitive rhodamine B detection. RSC Adv 11:21475–21488. https://doi.org/10.1039/d1ra02576g

56. Losso JN, Khachatryan A, Ogawa M, Godber JS, Shih F (2005) Random centroid optimization of phosphatidylglycerol stabilized lutein-enriched oil-in-water emulsions at acidic pH. Food Chem 92:737–744. https://doi.org/10.1016/j.foodchem.2004.12.029

57. Zhao HY, Liu S, He J, Pan CC, Li H, Zhou ZY, Ding Y, Huo D, Hu Y (2015) Synthesis and application of strawberry-like Fe_3O_4-Au nanoparticles as CT-MR dual-modality contrast agents in accurate detection of the progressive liver disease. Biomaterials 51:194–207. https://doi.org/10.1016/j.biomaterials.2015.02.019

58. Chen Q, Li K, Wen S, Liu H, Peng C, Cai H, Shen M, Zhang G, Shi X (2013) Targeted CT/MR dual mode imaging of tumors using multifunctional dendrimer-entrapped gold nanoparticles. Biomaterials 34:5200–5209. https://doi.org/10.1016/j.biomaterials.2013.03.009

59. Liu H, Li K, Wen S, Liu H, Peng C, Cai H, Shen M, Zhang G, Shi X (2013) Targeted tumor computed tomography imaging using low-generation dendrimer-stabilized gold nanoparticles. Chem - A Eur J 19:6409–6416. https://doi.org/10.1002/chem.201204612

60. Li J, Zheng L, Cai H, Sun W, Shen M, Zhang G, Shi X (2013) Facile one-pot synthesis of Fe_3O_4@Au composite nanoparticles for dual-mode MR/CT imaging applications. ACS Appl Mater Interfaces 5:10357–10366. https://doi.org/10.1021/am4034526

61. Xiao T, Wen S, Wang H, Liu H, Shen M, Zhao J, Zhang G, Shi X (2013) Facile synthesis of acetylated dendrimer-entrapped gold nanoparticles with enhanced gold loading

for CT imaging applications. J Mater Chem B 1:2773–2780. https://doi.org/10.1039/c3tb20399a

62. Ajeesh M, Francis BF, Annie J, Varma PRH (2010) Nano iron oxide-hydroxyapatite composite ceramics with enhanced radiopacity. J Mater Sci Mater Med 21:1427–1434. https://doi.org/10.1007/s10856-010-4005-9

63. Rotello V (2004) Nanoparticles building blocks for nanotechnology nanostructure science and technology. Nanostructure Sci. Technol. https://doi.org/10.1007/978-1-4419-9042-6